Chapter 18
THz Spectroscopy of Advanced Materials

Can Koral, Gianpaolo Papari, and Antonello Andreone

Abstract Materials research is an essential component of modern terahertz systems: novel, broadband, low loss and tunable devices all heavily rely on new materials, ranging from graphene to transition metal dichalcogenides and doped semiconductors. At the same time, terahertz spectroscopy provide a powerful tool for the characterisation of a broad range of materials, including composite polymers and biomolecules. In this review, we will present our recent progress on the use of time domain spectroscopy to extract microscopic information in an otherwise inaccessible portion of the electromagnetic spectrum.

18.1 Introduction

Due to its unique properties, the THz spectral regime is still out of reach of optical laser wavelengths, while at the same time standard high frequency electronics starts to fail. There is therefore an ever-expanding need for devices and systems operating at the THz frequencies that are efficient, tunable and broadband. Development of new and advanced materials can drive the rapid evolution of critical technologies like revolutionized information and telecommunication systems, highly efficient photovoltaic technologies and high colour contrast light emitting devices, among others. It is not farfetched that this demand would continually rise in the foreseeable future.

When used as a probe, the THz radiation can provide simultaneous and straightforward measure of the materials most fundamental properties, i.e. charge population

C. Koral
National Institute for Nuclear Physics, Naples Unit, Naples, Italy
e-mail: can.koral@na.infn.it

G. Papari · A. Andreone (✉)
Department of Physics, University of Naples "Federico II", Naples, Italy
e-mail: gianpaolo.papari@unina.it; andreone@unina.it

© Springer Nature B.V. 2021

M. F. Pereira, A. Apostolakis (eds.), *Terahertz (THz), Mid Infrared (MIR) and Near Infrared (NIR) Technologies for Protection of Critical Infrastructures Against Explosives and CBRN*, NATO Science for Peace and Security Series B: Physics and Biophysics, https://doi.org/10.1007/978-94-024-2082-1_18

dynamics, mobility, and the interplay between the two, which are not accessible to other optical or electrical techniques.

In this chapter, we will review our recent progress on the understanding of the electrodynamic parameters of some selected materials, potentially of interest for a number of different applications in the THz range, ranging from opto-electronics and bio-electronics to sensing.

18.1.1 ZnO Nanopowders

The large bandgap (3.3 eV) [1], visible light transparency, availability and multiple techniques for thin film deposition (chemical vapour deposition, sputtering, molecular beam epitaxy, etc.) make zinc oxide (ZnO) a versatile semiconductor extensively used in different technological applications [2, 3 and references therein]. Solar cells [4–10], piezoelectric actuators [11, 12] and thin film transistors are just a few examples of technological returns of ZnO. Different kind of doping have been applied to ZnO, aiming at improving conducting properties but preserving its transparency [8, 9, 13, 14]. Successful results have been reported in the attempt to dope ZnO with fluorine (F), since an additional electron with respect to oxygen is naively considered a "shallow donor" [2, 8, 9, 15]. Nevertheless, the mechanism through which F atoms can provide free carriers is still controversial [2, 16, 17]. Indeed, some authors predict an increase of extra delocalized electrons as well as overall carrier mobility due to F-doping [18, 19]. On the other hand, a decrease of conductivity of F-doped ZnO is expected by other studies [12].

Indeed, fluorine atoms are supposed to occupy oxygen vacancies that are the most favourable defects in ZnO_2. However, F atoms are theoretically expected to widen the distance between neighbouring Zn atoms, producing a deep localized state [2]. Density functional theory has been employed to account for the effect of fluorine doping on ZnO:F transport properties [16]. F atoms can work as either donor or acceptor according to the case they get full of oxygen vacancies or remain interstitials. The resulting activation energies have been estimated to be too high (~0.7 eV) for effectively providing any kind of carrier at room temperature, and the increase of free charge density could be ascribed to the effect of surface passivation operated by fluorine.

18.1.2 Graphene-Like Layers in Eumelanin

Graphene represents the first achievement of a fully two-dimensional material. A single sheet of carbon atoms is technologically versatile for its high ease of integrability [20–23] and fruitful electrodynamic properties in THz region, where it has been considered for the development of sensors [24, 25], filters [26], spatial light modulators [27–29], mantle cloaks [30]. Hybridized with organic based electronics

[31, 32], it has been extensively used for the production of novel biocompatible devices [33–36]. Within this frame the possibility to reproducibly fabricate graphene based nanowires and interfaces becomes quite relevant although only few attempts have been provided so far [37].

Recently, a reliable way for the realization of graphene micro-circuitry turned out to be the exploitation of graphene-like (GL) layers [38]. A GL layer is a platelet composed of a few layers of graphene having width of few nanometers. As a consequence of the manufacturing process, GL samples are born as water suspension, inherently predisposed to be molded in many shapes, and suitable for wiring organic electronics structures by spraying and/or ink-jet printing techniques either on rigid or flexible supports. An entire set of optical devices, including metamaterials, filters, absorbers, modulators, cloaks etc. can be newly proposed through the employment of the moldable GL compound. Analogously to some use of carbon nanotubes [39], a GL layer allows further interesting applications, to create new and cost-effective materials with tailored electrodynamic properties, for instance trough the mixture with specific insulating components.

Within the scenario of bio-electronics, eumelanin, a proved biocompatible material [40], can be exploited as an insulating sheath and host for GL layers in bioorganic environments.

18.1.3 Transition Metal Dichalcogenides

Transition metal dichalcogenides (TMDs) are characterized by a layered structure, responsible for their peculiar intrinsic 2-D electronic properties. Each crystal plane is based on the chemical configuration MX_2, where M is a metal and X is a chalcogen [41, 42]. Adjacent layers are held together by van der Waals forces, which inhibits free charge mobility across MX_2 planes. TMDs in thin-film form offer a large variety of compounds with adjustable band gaps [43, 44] and present a good transparency in the THz band that might pave the way to the development of a promising class of novel devices for THz optoelectronics [44]. Different from other tunable band gap systems like graphene, TMDs can also exploit an additional external parameter to control their own electro-optic properties as the magnetic field because of the spin-dependent band gap [45]. Furthermore, it has been shown [41, 46, 47] that the energy band structure of TMDs presents an interesting and unique dependence on the layer number, and a band gap transition from indirect to direct one for monolayer samples. Consequently, there is a consistent and growing demand in thin-film characterization, for the possible development of novel fast electronic [48, 49] and/or electro-optical systems [50, 51].

18.2 Sample Preparation and Structural Characterization

18.2.1 ZnO Nanopowders

Bare and F-doped ZnO powders were prepared by the hydrothermal route. Typically, a solution containing a 1:1 molar ratio of triethylamine (TEA) and zinc acetate di-hydrate (ZAD) was prepared, mixing TEA (0.84 mL) and ZAD (1.32 g) into ethanol (36.0 mL) under constant stirring. After complete dissolution of ZAD, water (4.0 mL) was added drop-wise, producing a whitish suspension. Afterwards, different amounts of ammonium hydrogen fluoride (NH_4FHF) were used to realize the following atomic F concentrations: 1 at%, 3 at%, and 5 at%. The obtained suspensions were sealed within a Teflon recipient (the liquid volume corresponding to 75% of the whole), placed into a circulating oven and kept at 120 °C overnight. After cooling down to room temperature, powders were recuperated by centrifugation and repeatedly washed (three times with distilled water). Prepared samples will be named thereafter F1, F3, F5, respectively. F0 indicates the undoped sample.

For the THz measurements, pellets of ZnO:F/KBr in the ratio 1:10 were opportunely realised. Samples roughly 330 μm thick were obtained by pressing a mixture of 90% of KBr powder with the 10% of ZnO:F. KBr was chosen because sufficiently transparent up to about 2.5 THz, behaving therefore as an optimal host for THz spectroscopy. This procedure gives the advantage to precisely control within a few microns the thickness of each sample that is a crucial parameter for THz spectroscopy.

18.2.2 GL and EUGL Pellets

GL layers were obtained applying a two-step oxidation/chemical reduction strategy described in a previous work [38]. A brief description of the applied method is as follows: 500 mg of Carbon Black (CB) powder was oxidized with nitric acid (67%, 10 mL) at 100 °C under stirring and reflux for 90 h. The oxidized carbonaceous material, labeled as GL-ox, was recovered by centrifugation and washed with distilled water until acid traces were successfully removed. After the oxidation step, 60 mg of GL-ox was dispersed in distilled water (60 mL) and treated with hydrazine hydrate (1.35 mL) of at 100 °C under reflux. After 24 h the suspension was cooled at room temperature and the excess of hydrazine was neutralized with an diluted nitric acid (4 M) allowing the precipitation of a black solid: the GL layers. GL layers were recovered by centrifugation (3000 rpm, 30 min), washed with distilled water and recovered again by centrifugation. This last purification step was repeated twice. The material was in part stored as aqueous suspension (mass concentration 1 mg mL-1, pH 3.5) and in part dried at 100 °C and stored. Analytical grade chemicals were purchased from Sigma Aldrich and used without any further

purification. CB (N110 type, furnace black, 15–20 nm primary particles diameter, specific BET area 139 $m^2\ g^{-1}$) was purchased from Sid Richardson Carbon Co.

Eumelanin was synthetized under biomimetic conditions through 5,6-dihydroxindole (DHI) and 2-carboxy-5,6-dihydroxindole (DHICA) oxidative co-polymerization [52]. DHI and DHICA were prepared according to a procedure previously described [53]. A mixture (3:1 in weight) of DHI/DHICA was dissolved in methanol (20 mg/mL) by ultrasonic agitation and the resulting suspension was kept for 10 min under magnetic stirring. The pH was adjusted to 8 with ammonia solution (28% in water) allowing indoles to auto-oxidize and polymerize. After 1 h, the reaction was quenched by adding acetic acid solution (1 M) until pH 4 is established. The material was then dried at 100 °C and stored as EU.

The hybrid material EUGL was prepared according to the procedure previously described [40]. Briefly, a proper amount of GL layers in aqueous suspension (1 mg mL^{-1}) was added to the mixture of eumelanin precursors (DHI/DHICA) dissolved in methanol before the addition of ammonia solution to induce the EU precursors oxidation and polymerization. The work-up of the reaction was the same as described for the preparation of pure eumelanin. The suspension was dried in an oven at 100 °C and stored. After drying the EUGL hybrid resulted insoluble in water.

Solid dispersions were prepared by mixing and grinding the samples with KBr (host) in different mass ratios (see [54] for details). The solid dispersions were compressed at 10 tons for 10 min into thin disks (13 mm in diameter) having thickness values ranging between 0.038 and 0.045 cm.

18.2.2.1 WSe_2 and $MoSe_2$ Films

TMD films have been deposited using a process known as thermally assisted conversion (TAC). TAC has the capability of depositing a continuous large-scale film with multiple layers [55]. The appropriate transition metal (Mo, W) films were deposited using a sputter coater (PECS, Gatan) at <2 Å/s to form a smooth conformal coating 10 nm thick on a c-axis SiO_2 substrate. In order to convert the metal films with their respective diselenides, they were exposed to selenium vapor at an elevated temperature in a home-built hot-wall chemical vapor deposition reactor with a process that has been described in more detail previously [43]. Specifically, metal films were converted to selenide in the reactor with chamber temperature at 600 °C under a flow of about 150 sscm of argon with the Se powder source held upstream at 219 °C for 2 h. Previous characterization indicated that the final thickness of selenide ($MoSe_2$, WSe_2) was 20 nm, which was double the initial metal thickness. To protect the films from oxidants in the atmosphere, they were encapsulated with 5 nm of Al_2O_3 using atomic layer deposition carried out over 46 cycles at 80 °C and a pressure of 2.2 Torr.

Using a shadow mask, samples were deposited on one half of SiO_2 c-axis substrates having a total area of 2 cm × 1 cm. The second half was intentionally left bare, so that one could retrieve the thin-film parameters employing the exact film thickness and refractive index $\widetilde{n}_s$ of the specific substrate on which each sample was

deposited. As it will be shown in detail in the next paragraphs, this was the only effective procedure to minimize the error introduced by the unavoidably slight difference in substrate parameters [56].

18.3 Experimental

THz spectroscopy measurements were carried out using a Time-Domain system based on a fs fiber system (Menlo Systems™). Generation and detection of THz signal is accomplished through the use of two photoconductive antennas based on GaBiAs semiconductor technology and excited by a laser pulse having 1560 nm wavelength and a repetition rate of 80 MHz. THz signal is collimated and then focalized on the sample using TPX (Polymethylpentene) lenses. The size of the Gaussian profile of the focused THz pulse, estimated with the standard knife-edge technique, is of the order of 2 mm. Temporal sampling rate is fixed at about 0.1 ps, whereas the whole acquisition interval ranges between 100 and 200 ps, giving a frequency resolution of about 5 GHz in the optimised conditions. The free space signal has a bandwidth extension up to about 4 THz, roughly halved in case of samples showing a high level of absorption. Samples are placed on an aluminum plate provided with circular holes 8 mm in diameter, as sketched in Fig. 18.1.

The holder is mounted on a two-dimensional motor stage, which enables to acquire measurements through free space, reference, and samples during the same run, with an enhanced accuracy on phase and amplitude for each single acquisition. In order to reduce or eliminate the effect of H_2O absorption in the frequency spectra, all measurements are performed in a purging box filled with N_2 and a humidity level lower than 0.1%.

18.4 Theoretical Background

Electrodynamic properties of powders, pellets and films have been studied by applying a standard approach based on the computation of the complex Transfer Function (TF) $\widetilde{T}(\omega)$ ($\omega = 2\pi f$), experimentally obtained through the ratio between the signal transmitted through the pellet $\widetilde{E}_s(\omega)$ and the signal collected in free space $\widetilde{E}_r(\omega)$.

In the case of bulk (optically thick) samples, the modulus of transmission can be expressed as

$$T(\omega) = \frac{E_S(\omega)}{E_R(\omega)} = \widetilde{t}_{as}\widetilde{t}_{sa}\ exp\left[-i(\widetilde{n}_s - \widetilde{n}_{air})\frac{\omega d}{c}\right] \cdot FP(\omega) \tag{18.1a}$$

where

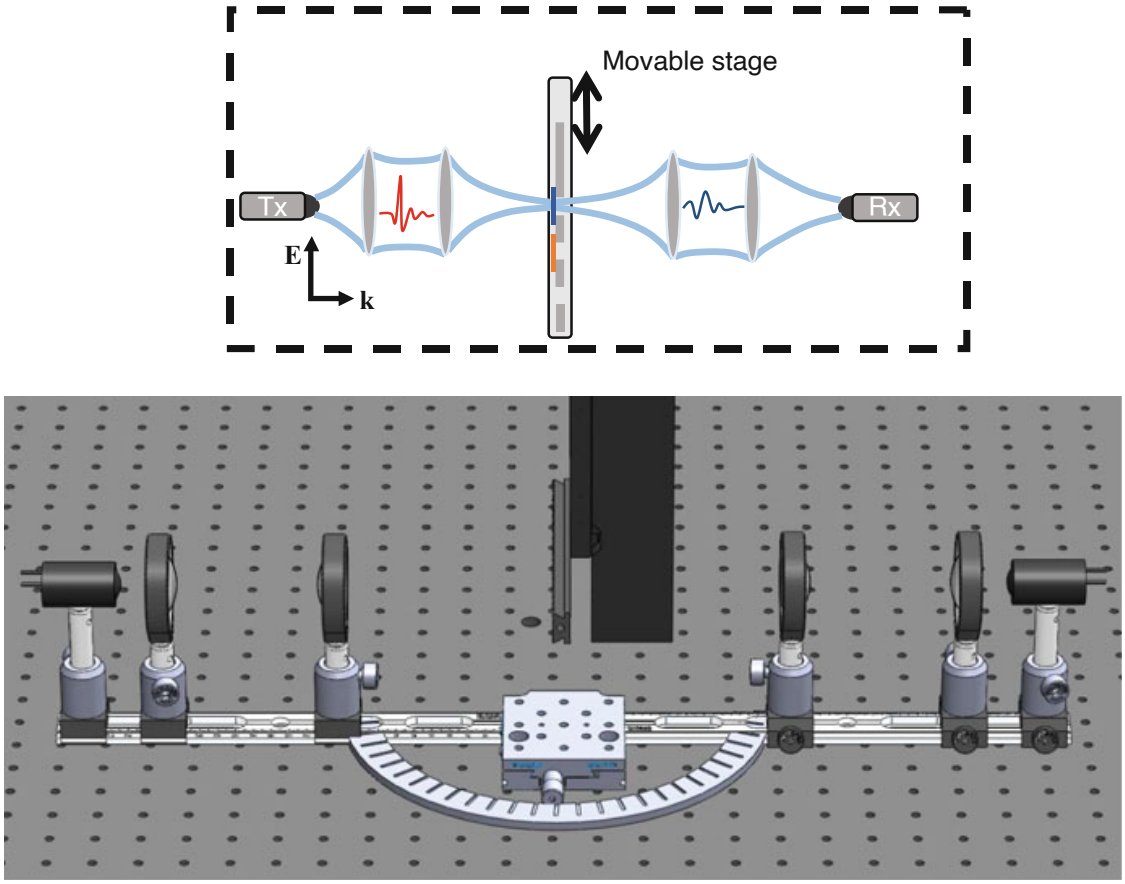

Fig. 18.1 Upper part: a sketch of the measurement scheme. Lower part: a pictorial representation of the optical setup. The THz radiation is collimated and then focalized, the holder can be moved so that the reference and different samples can be measured in the same experimental run

$$FP(\omega) = \frac{1}{1 - \left(\frac{\tilde{n}_{air}}{\tilde{n}_s + \tilde{n}_{air}}\right)^2 \exp\left(-i2\tilde{n}_s \frac{\omega d}{c}\right)} \tag{18.1b}$$

$\tilde{t}_{as}$ and $\tilde{t}_{sa}$ are the Fresnel coefficients at the boundaries air-sample and sample-air respectively, $\tilde{n}_s$ is the complex refractive index of the sample, $\tilde{n}_{air}$ the refractive index of air, d the sample thickness and c is the speed of light. The factor FP accounts for the oscillations due to the Fabry-Perot effect. A commercial software (Teralyzer™) has been used to achieve $\tilde{n}_s = n_s + ik_s$ for each single sample. This routine is based on *the total variation technique* [57–60] that defines the refractive index n_s, the extinction coefficient k_s, and the effective optical thickness d_{eff}, related to the minimum amplitude of FP oscillations. The effective optimal thickness is achieved with a precision of 2 μm.

The complex dielectric function $\tilde{\varepsilon}_s/\varepsilon_0 = \varepsilon_r + i\varepsilon_i$ is easily obtained through the relations $\varepsilon_r = n_s^2 - k_s^2$ and $\varepsilon_i = 2n_s k_s$ [61], with ε_0 as vacuum permittivity.

In order to extract the intrinsic value of the dielectric function of samples under test, we employed the mean field theory (Landau–Lifshitz–Looyenga model [62]). Briefly, we used the following formula

$$\widetilde{\varepsilon}_{\mathrm{g}}\left(\eta_{\mathrm{g}}\right)=\left(\widetilde{\varepsilon}_{\mathrm{s}}^{1/3}-\left(1-\eta_{\mathrm{g}}\right)\cdot\widetilde{\varepsilon}_{\mathrm{h}}^{1/3}\right)^{3}/\eta_{\mathrm{g}} \tag{18.2}$$

relating the guest substance permittivity $\widetilde{\varepsilon}_g$ to the permittivity of both the host substance $\widetilde{\varepsilon}_h$ (KBr) and sample (mixture) substance $\widetilde{\varepsilon}_s$. The coefficients $\eta_{g,\,h}$ represent the concentrations in volume of guest and host substance and are related to the experimental concentrations in weight α_g, through the equation:

$$\eta_g=\left(1+\frac{\rho_g}{\rho_h}\,\frac{1-\alpha_g}{\alpha_g}\right)^{-1} \tag{18.3}$$

with ρ_g and ρ_h mass density of the guest and host substance respectively.

For thin films deposited on a substrate having a refractive index $\widetilde{n}_{substr}$, it can be easily shown [68] that also this parameter has to be used in Eq. (18.1b), so that

$$FP(\omega)=\frac{1}{1-\left(\frac{\widetilde{n}-\widetilde{n}_{air}}{\widetilde{n}+\widetilde{n}_{air}}\right)\left(\frac{\widetilde{n}_s-\widetilde{n}_{substr}}{\widetilde{n}_s+\widetilde{n}_{substr}}\right)\exp\left(-i2\widetilde{n}_s\frac{\omega d}{c}\right)}$$

Permittivity and conductivity parameters in the following have been fitted using a conventional Drude-Smith model [63]. Complex permittivity can be written as

$$\widetilde{\varepsilon}(\omega)=\varepsilon_\infty-\left\{\frac{\omega_p^2}{\omega^2+i\omega\omega_\tau}\left(1+c_1\frac{\omega_\tau}{\omega_\tau-i\omega}\right)\right\} \tag{18.4}$$

where ε_∞ is the asymptotic value of ε_r, $\omega_p^2=ne^2/\varepsilon_0 m^*$ is the plasma frequency, n and m^* are the carrier density and effective mass respectively, and $\omega_\tau=1/\tau$ is the relaxation frequency. The coefficient c_1 ranges between -1 and 0 and accounts for the portion of localized/backscattered electrons. THz conductivity can be simply obtained through the expression

$$\widetilde{\sigma}(\omega)=-i[\widetilde{\varepsilon}(\omega)-\varepsilon_\infty]\varepsilon_0\omega \tag{18.5}$$

and from here the dc conductivity σ_{dc}, using

$$\sigma_{dc}=(1+c_1)\omega_p^2\varepsilon_0/\omega_\tau \tag{18.6}$$

18.5 THz Spectroscopy

18.5.1 ZnO

An expanded view on the measured time dependent THz signals is shown in Fig. 18.2, left panel, where the reference (free space), ZnO:F1/KBr, ZnO:F3/KBr and ZnO:F5/KBr sample curves are reported as solid lines with different colors. The average delay between the reference and the ZnO:F/KBr samples is mostly due to the contribution of the KBr which occupies the 90 wt.% of each pellet mixture. Instead, the effect of losses is more pronounced by comparing the transmission moduli $\left|\widetilde{T}(\omega)\right|$ as reported in Fig. 18.2, right panel. The average transmission amplitude undergoes a robust enhancement of about 50% passing from ZnO:F0 (not shown) to ZnO:F1. Increasing the doping level, $\left|\widetilde{T}(\omega)\right|$ in doped samples decreases, remaining anyway more transparent than pure ZnO. All samples display significant Fabry-Perot oscillations, whose periodicity [64] $\Delta f = \frac{c}{2n_p d} \approx 0.2\ THz$ yields a refractive index for a pellet $n_p \approx 2.3$, in agreement with the value achievable by temporal delay of THz signals $n_p = c\frac{\delta t}{d} + 1$ for $d \cong 330\ \mu m$ and $\delta t \cong 1.4\ ps$.

Following the theoretical approach described in the previous section, we have extracted the intrinsic $\widetilde{\varepsilon}$ for all samples. The real part of permittivity tends to increase passing from $\varepsilon_r \cong 10$ for ZnO:F0 (not shown) to $\varepsilon_r \cong 14$ for ZnO:F5 at 1 THz. Instead, ε_i describes more complicate dynamics as the doping increases. At 1 THz, the bare sample has $\varepsilon_i \cong 18$ whereas for ZnO:F1 the value drops at $\varepsilon_i \cong 10.5$, losing about 42% of its value. As the doping is further increased ε_i gets closer to the value of bare ZnO, although ZnO:F5 still has $\varepsilon_i \cong 15$. The sample conductivity can be easily gained through $\sigma(\omega) = \varepsilon_0 \omega \varepsilon_i(\omega)$, whose dependence on fluorine doping clearly follows the same dynamics as in ε_i. In Fig. 18.3, left and right panel respectively, the real part of the dielectric function ε_r and the THz conductivity σ are reported as a function of frequency in the left and right panel respectively.

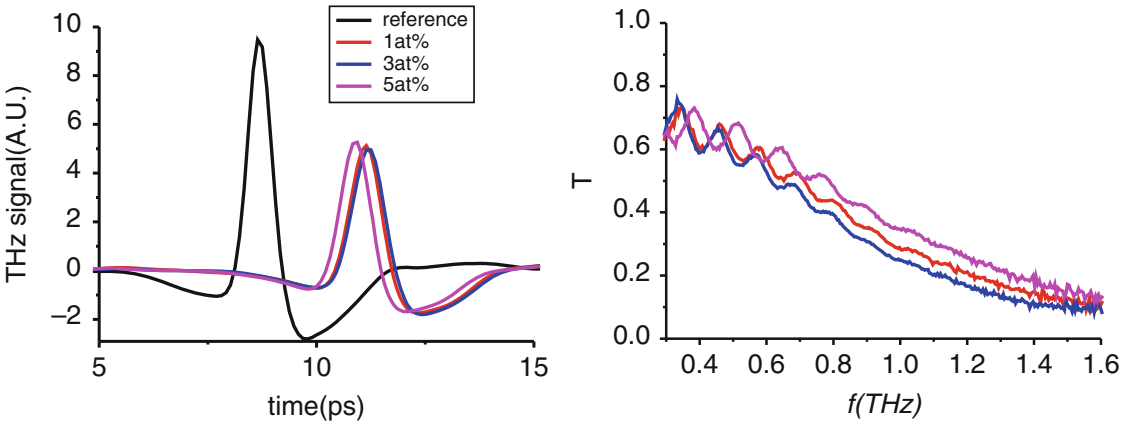

Fig. 18.2 Left: Electric field signals versus time transmitted in free space (black curve) and through the ZnO:F/KBr samples under test. Right: Corresponding transmission versus frequency. Samples having 1 at%, 3 at% and 5 at% fluorine are represented by the red, blue and magenta solid lines respectively

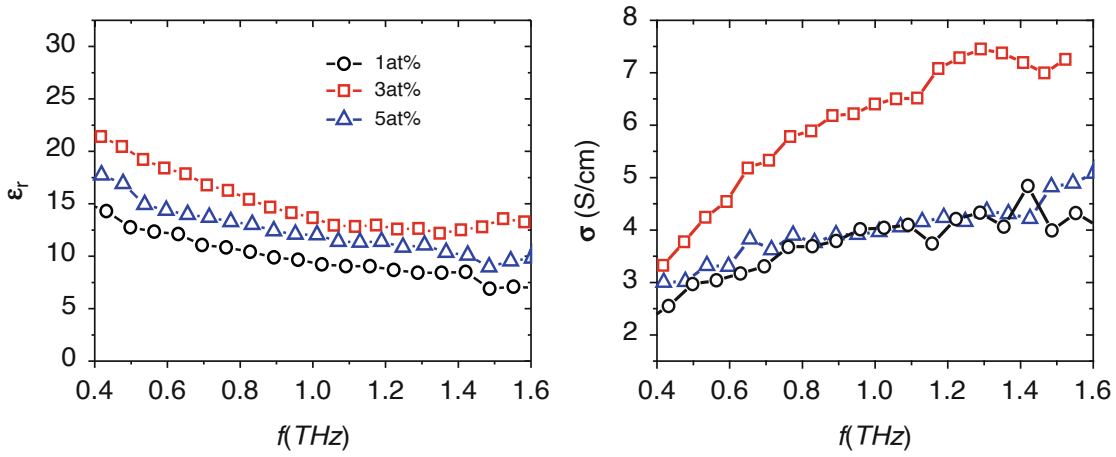

Fig. 18.3 Left: relative permittivity (ε_r) vs *f*. Right: conductivity (σ) vs *f*. Experimental data for the ZnO:F samples are plotted via circles, squares, and triangles corresponding to fluorine percentage of 1 at.%, 3 at.% and 5 at.% respectively

Table 18.1 Parameters used for the best fit of the ZnO:F powders complex permittivity according to the Drude-Smith model. The uncertainty of tabled parameters is of the order of 2% (taken from [66])

Sample	ω_p (*THz*)	ω_τ (*THz*)	C_1	σ_{dc} (S/cm)	ε_∞
F0	49	10	−0.70	6.4	10
F1	49	13	−0.85	2.4	9.5
F3	50	13	−0.83	2.9	11
F5	50	11	−0.8	4.0	12

Taking as a reference the extracted direct conductivity, we can quantify the decrease of ZnO:F transport properties, noting that at 1 THz we find: $\sigma_{dc}(ZnO:F1) \times 2.7 \cong \sigma_{dc}(ZnO:F0)$ and $\sigma_{dc}(ZnO:F5) \times 1.6 \cong \sigma_{dc}$.

THz and *dc* conductivity of the bare sample are in agreement with similar measurements performed on zinc oxide thin films [13, 65]. Instead, THz conductivity of ZnO:F1 undergoes a relevant decrease passing from about 10 S/cm, in the absence of doping, to about 6 S/cm. In order to find more quantitative information on the intrinsic conductivity we have fitted for all samples $\widetilde{\varepsilon}$ with the Drude-Smith model (Eq. 18.4). The extracted parameters, which are affected by an uncertainty of about 2%, are summarized in Table 18.1.

According to the Drude-Smith model, specifically developed to account for the rate of backscattering processes in granular systems, the conductivity decreases because of the simultaneous increase of $|c_1|$ and relaxation time ω_τ (Eq. 18.6). Indeed, both parameters increase by more than 20% in ZnO:F1 and ZnO:F3. In ZnO:F5, instead, this increase is of the order of 10% only, in spite of a relevant decrease of its conductivity in comparison with the bare sample. The lowering of conductivity can be better accounted for by looking at the change in morphology of ZnO:F powders, as shown by SEM analysis. The growth of $|c_1|$ is coherent with a system in which the number of grain boundaries involved into the relaxation process

increases. Since the relative variation of relaxation time $\omega_\tau = 1/\tau$ follows the variation in $|c_1|$, we can infer that the Mattheissen's rule [67] $1/\tau = 1/\tau_i + 1/\tau_{gb}$ holds. Here τ_i accounts for the relaxation process inside a single grain and τ_{gb} relates to the average scattering time at grain boundaries. As fluorine doping is increased, the change in morphology suggests that τ_{gb} decreases, so that ω_τ basically follows the change in ω_{gb}.

The consequences of an effective doping mechanism would reflect into a strong enhancement of ω_p because of the growth of carrier density. Instead, we observe a slight upshift of about 2%, hardily explainable in terms of an effective doping mechanism. On the other hand, the real part of permittivity tends to grow as a function of doping, and the reference value ε_∞ in ZnO:F5, is about 20% larger than the bare value. This is the signature of some localized (polarizable) charge provided by the doping process. The enhancement of ε_∞ is reasonably ascribable to the enhancement of luminescence centers observed in PL measurements too.

We can therefore summarize the most significant information extracted using THz spectroscopy from ZnO:F samples, as a function of the doping increase:

σ_{dc} first decreases and then increases again, however never restoring the value of the bare sample;
both $|c_1|$ and ω_τ reasonably increase for the rise of scattering rate at grain boundaries;
ω_p remains basically constant, and ε_∞ tends to increase.

It is remarkable to note that the above Drude-Smith parameters keep their significance and trends within the highest uncertainty inherited from $\widetilde{\varepsilon}$.

We infer therefore that the fluorine doping slightly affects the polarization charge of ZnO:F powders but does not enhance the carrier density. ZnO:F samples instead show a granular morphology at nanoscale, compatible with the growth of the grain boundary scattering rate and the decrease of σ_{dc}. The increase of the fraction of smaller particles with the amount of doping precursor can explain this effect.

18.5.2 GL and EUGL

Again, the time dependent evolution of the electric field transmitted through different samples is recorded and compared with the reference (air) signal. From here, meaningful information on the electrodynamic parameters of the samples under text can be derived from the frequency transmission T(ω) in the range 0.1–2 THz. Results for GL/KBr mixtures are reported in Fig. 18.4 for various volume concentrations. Increasing the content of GL in KBr, THz losses increase accordingly, so that the amplitude scales down and is frequency limited by the lower Signal-to-Noise Ratio (SNR). Therefore, in pure KBr T(ω) extends to 2 THz, whereas for maximum GL layers concentration (approximately 10%) a significant signal is observed up to 1 THz only.

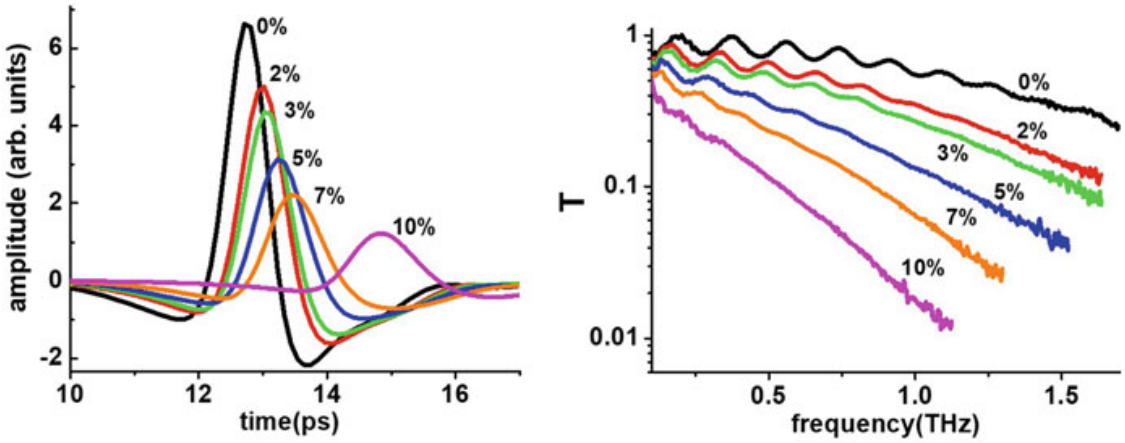

Fig. 18.4 Left: Time dependent evolution of the transmitted THz signal as a function of different GL concentration. Black: 0% (pure KBr); red: 2%; green: 3%; blue: 5%; orange: 7%; magenta: 10%. Percentages refer to the concentration of GL in the KBr matrix. Right: T as a function of frequency for the same samples

We first use THz spectroscopy to capture changes in the electrodynamic parameters obtained through chemical transformations of compounds GL and EUGL layers are based on.

Then, the technique is applied to highlight the differences in the electrodynamic behavior of simple mixtures of eumelanin and graphene-like layers (EU + GL) and the hybrid obtained through their polymerization (EUGL) (for details, refer to [54]).

Polymerization induces EU to incorporate GL layers into nanodrops having an average diameter of few tenths of nanometers [38]. This has incisively affected the percolation path when compared to the case of a simple mixture between EU and GL layers. If the polymerization helps also the onset of new chemical bonds that may degrade GL conductivity, it remains an issue that has not been addressed yet.

Using the retrieval procedure, we can finally extract the complex permittivity and the effective thickness of pure KBr and mixed samples of GL and EUGL layers. Once $\widetilde{\varepsilon}_h$, the complex permittivity of the host substance (KBr), and $\widetilde{\varepsilon}_s\left(\alpha_g\right)$ have been retrieved, $\widetilde{\varepsilon}_g\ (\alpha_g)$ is obtained employing Eqs. (18.2) and (18.3). At 1 THz we find $\varepsilon_r(KBr) \cong 5$ and $\sigma_r(KBr) \cong 0.4\ S/cm$, in substantial agreement with results reported in [68].

A summary of the results on the real and imaginary parts of the dielectric function as a function of frequency and the conductivity for two representative GL and EUGL samples are reported in Fig. 18.5.

In the GL sample, both ε_r and ε_i strongly decrease in the frequency range 0.3–1.5 THz. In comparison, the hybrid EUGL displays similar frequency dependence for ε_r, with smaller values but at the highest frequencies. The behavior of ε_i instead is quite different, with nearly flat frequency dependence and absolute values reduced by a factor 5 or more.

Quantitative insights on the complex dielectric function $\widetilde{\varepsilon}$ of both GL and EUGL compounds can be retrieved using a simple Drude-Smith model through Eqs. (18.4) and (18.5). We found reasonable parameters by fitting *simultaneously* the families of

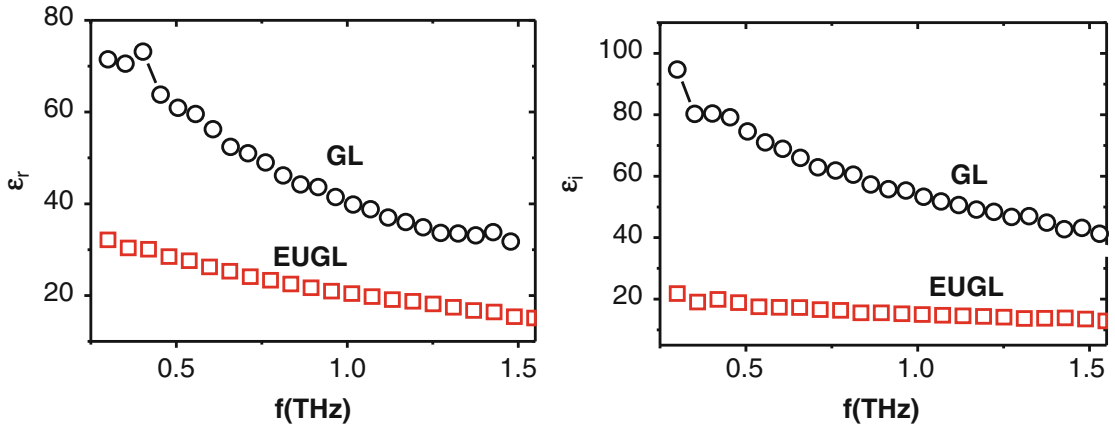

Fig. 18.5 In the panels the real (left) and imaginary (right) components of the permittivity as a function of frequency for two different samples (graphene-like, GL: black circles; hybrid graphene-like + eumelanin, EUGL: red squares) are shown

Table 18.2 List of parameters used for fitting ε_r and σ data through Drude-Smith model for the GL and EUGL mixtures. The last two columns account for the total uncertainty relative to $\widetilde{\varepsilon}$ and σ_r obtained through data dispersion (taken from [54])

Sample	ω_p (*THz*)	ω_τ (*THz*)	C_1	σ_{dc} (S/cm)	ε_∞	$\delta\varepsilon$	$\delta\sigma$
GL	82.9	1.6	−0.75	15	32	15%	10%
EUGL	50.2	1.8	−0.85	2.9	18	13%	10%

curves $\varepsilon_r(\eta_g)$ and $\varepsilon_i(\eta_g)$ of both GL and EUGL samples. Drude-Smith model implies the knowledge of 4 parameters that are summarized in Table 18.2. Through Eq. (18.6) we get as direct conductivities σ_{dc} =15 S/cm and σ_{dc} =2.9 S/cm for GL and EUGL respectively. The total uncertainty relative to the complex permittivity ($\delta\varepsilon$) and conductivity ($\delta\sigma$) are worth 15%(13%) and 10%(10%) for GL (EUGL) samples. Specifically the permittivity uncertainty has been calculated by the spread of $\widetilde{\varepsilon}$ as function of concentration η_g so that $\delta\varepsilon = \sqrt{\delta\varepsilon_r{}^2 + \delta\varepsilon_i{}^2}$, whereas $\delta\sigma$ just relies on the data spread detected into plotting σ_r (η_g).

GL and EUGL appear sharply different in terms of σ_{dc} and ε_∞ because we find σ_{dc} (GL) ≅5 σ_{dc} (EUGL), and 1.77 ε_∞ (EUGL) ≅ε_∞ (GL). Also ω_p values are well separated within $\delta\varepsilon$ interval whereas ω_τ values, describing the time scale of photoconduction, are comparable within the total uncertainty ($\delta\varepsilon$), because of the dependence of both on conductive properties of GL. Amplitudes of σ_{dc} are suppressed by the factor $1 + c_1$ which limits to less than 30% the fraction of carriers available for direct conduction. GL and EUGL display photoconductive properties similar to the amorphous carbon [69], that are a few times lower than the performances of carbon nanotubes compound [70] and a factor 1000 lower than performances of graphene based systems [71]. Charge densities of GL and EUGL are slightly lower than carbon nanotubes, indeed being $n = \omega_p^2 m^* \varepsilon_0 / e^2$ we get n $(GL) \cong 2 \cdot 10^{18}/cm^3$ and $n(EUGL) \cong 2 \cdot 10^{17}/cm^3$ having employed $m^* = 0.87\ m_e$ the effective mass of charges in carbon amorphous samples [72].

18.5.3 TMD

In Fig. 18.6 the temporal evolution of the electric field signals transmitted across the WSe_2 (left panel) and $MoSe_2$ (right panel) samples is reported. Black curves represent the free space transmission, whereas red curves refer to signals passing through the bare substrate. Peak amplitude in the substrate was always around 20% lower than the free space case, and its delay of about $\delta t \approx 2$ ps described the proper change in refractive index (since the nominal thickness was 300 μm, this corresponds to $n_s \approx 2$ for the crystalline SiO_2). The presence of the WSe_2 and $MoSe_2$ thin-film induced a further reduction in the transmitted signal (blue curves) of about 30% and 10%, respectively, when compared to the bare substrate. In all cases, THz waves impinging and passing through each sample caused an etalon effect with the first reflected signal manifesting itself with a delay of almost 5 ps from the main peak.

Time dependent signals were then converted in the frequency domain using a fast Fourier transform (FFT) method to get the transmission function $\widetilde{T}(\omega) = \widetilde{E}_f(\omega)/\widetilde{E}_s(\omega)$, where the complex quantities $\widetilde{E}_f(\omega)$ and $\widetilde{E}_s(\omega)$ are the FFT curves of the sample and bare substrate, respectively.

Results are presented in Fig. 18.7 in terms of the real and imaginary part of the complex dielectric function.

The real part ε_r (left panel) displays substantially a flat dynamics, with $MoSe_2$ characterized by a very high dielectric constant (≈1000) and WSe_2 values being slightly negative. Imaginary parts ε_i of the two films are reported in the right panel, showing the expected free-charge decrease, although values for ε_i (WSe_2) were larger than for ε_i ($MoSe_2$) by a factor of 5 or more. The $MoSe_2$ film, therefore, showed a semiconducting behavior with the real part being strictly positive and a fast decay of ε_i versus frequency [67]. On the other hand, the WSe_2 sample clearly presented a weak metallic behavior in the THz region, showing a complete negative ε_r and large values for ε_i.

Fitting curves on the retrieved dielectric functions of WSe_2 and $MoSe_2$ films, obtained via the DS model, are reported as continuous black lines in the same

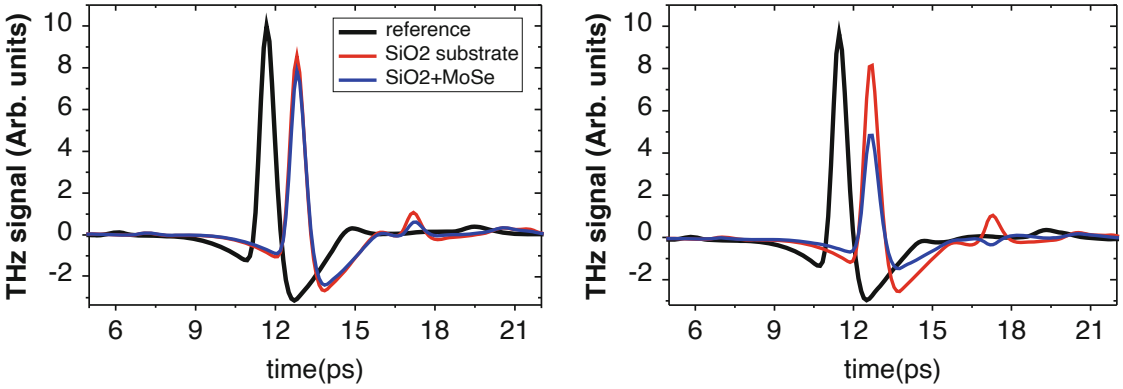

Fig. 18.6 Left: Black, red and blue solid lines represent the time dependent THz signals referred to free space, SiO_2 substrate and WSe_2 film + substrate respectively. Right: Similarly, with the blue curve showing the measurement on the $MoSe_2$ film + substrate

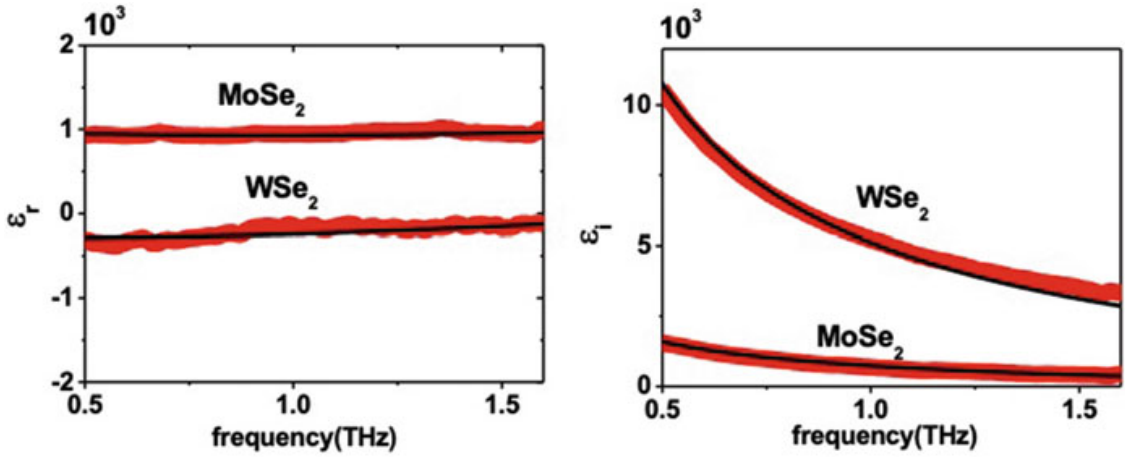

Fig. 18.7 Left and right graphs show the real (ε_r) and imaginary (ε_i) parts respectively of dielectric function of TMD's films as a function of frequency, extracted by using the Transfer Function model. Black lines corresponds to the Drude-Smith model fits whose parameters are reported in Table 18.3

Table 18.3 Best fit parameters for the dielectric functions of WSe_2 and $MoSe_2$ films using the Drude-Smith model. Parameter accuracy is of the order of 5% (taken from [75])

Sample	ω_p (*THz*)	ω_τ (*THz*)	C_1	σ_{dc} (S/cm)	ε_∞
WSe_2	850	16	−0.22	3000	1200
$MoSe_2$	270	9.5	−0.35	444	1220

figures. The used fitting parameters are reported in Table 18.3, with an uncertainty of about 5%. The higher conductivity of WSe_2 with respect to $MoSe_2$ mainly resulted in larger values of ω_p and smaller values of c_1, as expected.

Nevertheless, the frequency response of the dielectric function and the values retrieved for the d.c. conductivity using the DS model was in clear contrast to what is observed in single crystal samples [73]. The observed metallic behavior may be ascribed to the presence of conductive channels in grain boundaries. A high density of metallic grain boundaries can in fact spontaneously form in slightly Se-deficient Mo thin films grown by molecular-beam epitaxy [74]. We speculate that the same mechanism may apply to WSe_2 samples. This would also explain the larger values of conductivity in the latter case.

Before we proceed to concluding remarks, we would like to mention that there are other materials also being investigated for spectroscopy and devices in the THz range, notably based on superlattices and quantum-cascade structures [76–88].

18.6 Conclusions

Our results on fluorine doped ZnO powders prepared through hydrothermal synthesis show that F atoms do not work as donors but rather affect the morphology of ZnO crystals only, promoting the onset of a granular phase. Electron paramagnetic resonance (EPR) and photoluminescence (PL) measurements [66] proved the effective F doping of ZnO structures, showing that, increasing the doping level up to 5%, F atoms mainly occupy oxygen vacancies, inherently present in the bare ZnO. The increase of luminescence centers revealed via PL data well corresponds to the rise of asymptotic permittivity detected by THz spectroscopy. THz TDS measurements confirm that ZnO:F powders do not show an increment in free carrier charge. Indeed, the doping precursor exerts a relevant leaching on ZnO mesocrystals, leading to an increase of the fraction of smaller nanoparticles and, consequently, of scattering rate at grain boundaries, that ultimately affects conductivity. Our outcomes are in accordance with theoretical calculations asserting it is not possible to provide free carriers in ZnO through F doping at room temperature. Experimental verification of free charge enhancement in ZnO thin films can be reasonably related to a different role played by F atoms, which can work as passivation layer preserving the intrinsic conductivity of zinc oxide.

We have also performed a detailed THz investigation on the high frequency electrodynamics in graphene-like and eumelanin-graphene-like layers. Samples have been hosted in KBr powder with different concentrations. Intrinsic values of $\widetilde{\varepsilon}$ have been achieved through a Landau-Lifshitz approach. Above the percolation concentration, all data converge inside specific areas in $\widetilde{\varepsilon}$ vs frequency space, allowing to get with a reasonable precision information – using a simple Drude-Smith model - on the electrodynamic parameters of both hybrids in this frequency range. Measured values of conductivity are encouraging and open the possibility to employ GL and EUGL compounds for the development of bio-compatible circuitry and devices working up to the THz range.

Finally, we have retrieved the dielectric function of conducting $MoSe_2$ and WSe_2 TMDs. Thin films have been created via a thermally assisted conversion process, which produced samples with good homogeneity. We have extracted the electrodynamic parameters of thin films deposited on 300 μm thick substrates, which introduce a relatively strong FP effect in transmission data. By applying a rigorous protocol based on the TF model and a self-consistent moving average procedure, we have minimized the periodic FP oscillations and fitted $\widetilde{\varepsilon}$ with the Drude–Smith function. The relatively high conductivity observed in both compounds may be ascribed to a high density of line defects presenting a metallic character. The relatively high transparence along with the conducting features are encouraging in view of a possible use of TMD-based thin-films for applications as tunable metadevices in the THz region. The observed conducting nature can represent a promising alternative for the realization of new devices with higher currents and lower contact resistance.

Acknowledgments We acknowledge many authors for samples preparation and characterisation: M. Alfè, L. De Stefano, V. Gargiulo, and I. Rea from the National Research Council (CNR) of Italy; A. Aronne, R. Di Capua, G. Luciani, A. Pezzella, B. Silvestri, and G. Vitiello from the University of Naples "Federico II", Naples, Italy; T. Hallam and G. S. Duesberg from Trinity College, Dublin, Ireland.

We further acknowledge the support of the National Institute for Nuclear Physics (INFN) under the Project "Terahertz ERA".

References

1. Mang A, Reimann K, Rübenacke S (1995) Band gaps, crystal-field splitting, spin-orbit coupling, and exciton binding energies in ZnO under hydrostatic pressure. Solid State Commun 94:251
2. Janotti A, Van de Walle CG (2009) Fundamentals of zinc oxide as a semiconductor. Rep Prog Phys 72:126501
3. Ozgur U, Alivov YI, Liu C, Teke A, Reshchikov MA, Dogan S, Avrutin V, Cho SJ, Morkoc HA (2005) Comprehensive review of ZnO materials and devices. J Appl Phys 98:1
4. Azarang M, Shuhaimi A, Yousefi R, Sookhakian M (2014) Effects of graphene oxide concentration on optical properties of ZnO/RGO nanocomposites and their application to photocurrent generation. J Appl Phys 116:084307
5. Saáedi A, Yousefi R, Jamali-Sheini F, Zak AK, Cheraghizade M, Mahmoudian MR, Baghchesara MA, Dezaki AS (2016) XPS studies and photocurrent applications of alkali-metals-doped ZnO nanoparticles under visible illumination conditions. Physica E Low Dimens Syst Nanostruct 79:113
6. Dezfuly RF, Yousefi R, Jamali-Sheini F (2016) Photocurrent applications of $Zn_{(1-x)}Cd_xO$/rGO Nanocomposites. Ceram. Int 42:7455
7. Kharatzadeh A, Jamali-Sheini F, Yousefi R (2016) Excellent Photocatalytic performance of $Zn_{(1-x)}Mg_xO$/rGO Nanocomposites under natural sunlight irradiation and their photovoltaic and UV detector applications. Mater Des 107:47
8. Gordon RG (1997) Deposition of transparent conducting oxides for solar cells. AIP conference proceedings, pp 39–48
9. Liang H, Gordon RG (2007) Atmospheric pressure chemical vapor deposition of transparent conducting films of fluorine doped zinc oxide and their application to amorphous silicon solar cells. J Mater Sci 42:6388
10. Tari O, Aronne A, Addonizio ML, Daliento S, Fanelli E, Pernice P (2012) Sol–gel synthesis of ZnO transparent and conductive films: A critical approach. Sol Energy Mater Sol Cells 105:179
11. Li T, Li YT, Qin WW, Zhang PP, Chen XQ, Hu XF, Zhang W (2015) Piezoelectric size effects in a zinc oxide micropillar. Nanoscale Res Lett 10:394
12. Zhang Y, Liu C, Liu J, Xiong J, Liu J, Zhang K, Liu Y, Peng M, Yu A, Zhang A, Zhang Y, Wang Z, Zhai J, Wang ZL (2016) Lattice strain induced remarkable enhancement in piezoelectric performance of ZnO-based flexible nanogenerators. ACS Appl Mater Interfaces 8:1381–1387
13. Benramache S, Belahssen O, Temam HB (2014) Effect of band gap energy on the electrical conductivity in doped ZnO thin film. J Semicond 35:73001
14. Addonizio ML, Aronne A, Daliento S, Tari O, Fanelli E, Pernice P (2014) Sol–gel synthesis of ZnO transparent conductive films: the role of pH. Appl Surf Sci 305:194
15. Liu L, Mei Z, Hou Y, Liang H, Azarov A, Venkatachalapathy V, Kuznetsov A, Du X (2015) Fluorine doping: A feasible solution to enhancing the conductivity of high-resistance wide bandgap Mg0.51Zn0.49O active components. Sci Rep 5:15516

16. Liu B, Gu M, Liu X, Huang S, Ni C (2010) First-principles study of fluorine-doped zinc oxide. Appl Phys Lett 97:1
17. Zhang SB, Wei S-H, Zunger A (2001) Intrinsic N-type versus P-type doping asymmetry and the defect physics of ZnO. Phys Rev B 63:75205
18. Choi Y-J, Park H-H (2014) A simple approach to the fabrication of fluorine-doped zinc oxide thin films by atomic layer deposition at low temperatures and an investigation into the growth mode. J Mater Chem C 2:98
19. Lee HB, Ginting RT, Tan ST, Tan CH, Alshanableh A, Oleiwi HF, Yap CC, Jumali MHH, Yahaya M (2016) Controlled defects of fluorine-incorporated ZnO nanorods for photovoltaic enhancement. Sci Rep 6:32645
20. Liang G, Hu X, Yu X, Shen Y, Li HL, Davies AG, Linfield EH, Hou Kun Liang HK, Zhang Y, Yu SF, Wang QJ (2015) Integrated terahertz graphene modulator with 100% modulation depth. ACS Photonics 2:1559
21. Docherty CJ, Johnston MB (2012) Terahertz properties of graphene. J Infrared Milli Terahz Waves 33:797
22. Chen Z, Ren W, Gao L, Liu B, Pei S, Cheng H-M (2011) Three-dimensional flexible and conductive interconnected graphene networks grown by chemical vapour deposition. Nat Mater 10:424
23. Schwierz F (2010) Graphene transistors. Nat Nano 5:487
24. Sun J, Muruganathan M, Mizuta H (2016) Room temperature detection of individual molecular physisorption using suspended bilayer graphene. Sci Adv 2:e150151
25. Vicarelli L, Vitiello MS, Coquillat D, Lombardo A, Ferrari AC, Knap W, Polini M, Pellegrini V, Tredicucci A (2012) Graphene field-effect transistors as room-temperature terahertz detectors. Nat Mater 11:865
26. Danaeifar M, Granpayeh N, Mohammadi A, Setayesh A (2013) Graphene-based tunable terahertz and infrared band-pass filter. Appl Opt 52:E68
27. Sensale-Rodriguez B, Yan R, Kelly MM, Fang T, Tahy K, Hwang WS, Jena D, Liu L, Xing HG (2012) Broadband graphene terahertz modulators enabled by intraband transitions. Nat Commun 3:780
28. Lee SH, Choi M, Kim T-T, Lee S, Liu M, Yin X, Choi HK, Lee SS, Choi C-G, Choi S-Y, Zhang X, Min B (2012) Switching terahertz waves with gate-controlled active graphene metamaterials. Nat Mater 11:936
29. Kakenov N, Takan T, Ozkan VA, Balcı O, Polat EO, Altan H, Kocabas C (2015) Graphene-enabled electrically controlled terahertz spatial light modulators. Opt Lett 40:1984
30. Chen P-Y, Alú, A. (2011) Atomically thin surface cloak using graphene monolayers. ACS Nano 7:5855
31. Yoo D, Kim J, Kim JH (2014) Direct synthesis of highly conductive poly(3,4-ethylenedioxythiophene):poly(4-styrenesulfonate) (PEDOT:PSS)/graphene composites and their applications in energy harvesting systems. Nano Res 7:717
32. Park JW, Jang J (2015) Fabrication of graphene/free-standing nanofibrillar PEDOT/P (VDF-HFP) hybrid device for wearable and sensitive electronic skin application. Carbon 87:275
33. Cohen-Karni T, Qing Q, Li Q, Fang Y, Lieber CM (2010) Graphene and nanowire transistors for cellular interfaces and electrical recording. Nano Lett 10:1098
34. Liu Q, Guo B, Rao Z, Zhang B, Gong JR (2013) Strong two-photon-induced fluorescence from Photostable, biocompatible nitrogen-doped Graphene quantum dots for cellular and deep-tissue imaging. Nano Lett 13:2436
35. He Q, Wu S, Gao S, Cao X, Yin Z, Li H, Chen P, Zhang H (2011) Transparent, flexible, all-reduced graphene oxide thin film transistors. ACS Nano 5:5038
36. Liu Y, Yu D, Zeng C, Miao Z, Dai L (2010) Biocompatible graphene oxide-based glucose biosensors. Langmuir 26:6158

37. Tosic D, Markovic Z, Jovanovic S, Prekodravac J, Budimir M, Kepic D, Holclajtner-Antunovic I, Dramicanin M, Todorovic-Markovic B (2016) Rapid thermal annealing of nickel-carbon nanowires for graphene nanoribbons formation. Synth Met 218:43
38. Alfè M, Gargiulo V, Di Capua R, Chiarella F, Rouzaud J-N, Vergara A, Ciajolo A (2012) Wet chemical method for making graphene-like films from carbon black. ACS Appl Mater Interfaces 4:4491
39. Casini R, Papari G, Andreone A, Marrazzo D, Patti A, Russo P (2015) Dispersion of carbon nanotubes in melt compounded polypropylene based composites investigated by THz spectroscopy. Opt Express 23:18182
40. Gargiulo V, Alfè M, Di Capua R, Togna AR, Cammisotto V, Fiorito S, Musto A, Navarra A, Parisi S, Pezzella A (2015) Supplementing p-systems: eumelanin and graphene-like integration towards highly conductive materials for the mammalian cell culture bio-interface. J Mater Chem B 3:5070
41. Wang QH, Kalantar-Zadeh K, Kis A, Coleman JN, Strano MS (2012) Electronics and optoelectronics of two-dimensional transition metal dichalcogenides. Nat Nanotechnol 7:699
42. Jariwala D, Sangwan VK, Lauhon LJ, Marks TJ, Hersam MC (2014) Emerging device applications for semiconducting two-dimensional transition metal dichalcogenides. ACS Nano 8:1102–1120
43. Gatensby R, Hallam T, Lee K, McEvoy N, Duesberg GS (2016) Investigations of vapour-phase deposited transition metal dichalcogenide films for future electronic applications. Solid State Electron 125:39
44. Chen Y, Xi J, Dumcenco DO, Liu Z, Wang D, Shuai Z, Huang Y, Xie L (2013) Tunable band gap in atomically thin transition-metal Dichalcogenide alloys. ACS Nano 7:4610
45. Xu X (2014) Spin and pseudospins in transition metal dichalcogenides. Nat Phys 10:343
46. Guo HY, Lu N, Wang L, Wu XJ, Zeng XC (2014) Tuning electronic and magnetic properties of early transition-metal dichalcogenides via tensile strain. J Phys Chem C 118:7242
47. Li Y, Tongay S, Yue Q, Kang J, Wu J, Li J (2013) Metal to semiconductor transition in metallic transition metal dichalcogenides. J Appl Phys 114:174307
48. Docherty CJ, Parkinson P, Joyce HJ, Chiu M-H, Chen C-H, Lee M-Y, Li L-J, Herz LM, Johnston MB (2014) Ultrafast transient terahertz conductivity of monolayer MoS_2 and WSe_2 grown by chemical vapor deposition. ACS Nano 8:11147
49. Lui CH, Frenzel AJ, Pilon DV, Lee YH, Ling X, Akselrod GM, Kong J, Gedik N (2014) Trion-induced negative photoconductivity in monolayer MoS_2. Phys Rev Lett 113:166801
50. Tian H, Chin ML, Najmaei S, Guo Q, Xia F, Wang H, Dubey M (2016) Optoelectronic devices based on two-dimensional transition metal dichalcogenides. Nano Res 1:1543–1560
51. Sun Z, Martinez A, Wang F (2016) Optical modulators with 2D layered materials. Nat Photonics 10:227
52. D'Ischia M, Wakamatsu K, Napolitano A, Briganti S, Garcia-Borron JC, Kovacs D, Meredith P, Pezzella A, Picardo M, Sarna T, Simon JD, Ito S (2013) Melanins and melanogenesis: methods, standards, protocols. Pigment Cell Melanoma Res 26:616–633
53. Edge R, D'Ischia M, Land EJ, Napolitano A, Navaratnam S, Panzella L, Pezzella A, Ramsden CA, Riley PA (2006) Dopaquinone redox exchange with dihydroxyindole and dihydroxyindole carboxylic acid. Pigment Cell Res 19:443
54. Papari GP, Gargiulo V, Alfè M, Di Capua R, Pezzella A, Andreone A (2017) THz spectroscopy on graphene-like materials for bio-compatible devices. J Appl Phys 121:145107
55. Gatensby R, McEvoy N, Lee K, Hallam T, Berner NC, Rezvani E, Winters S, O'Brien M, Duesberg GS (2014) Controlled synthesis of transition metal dichalcogenide thin films for electronic applications. Appl Surf Sci 297:139
56. Walther M, Cooke DG, Sherstan C, Hajar M, Freeman MR, Hegmann FA (2007) Terahertz conductivity of thin gold films at the metal-insulator percolation transition. Phys Rev B 76:125408
57. Pupeza I, Wilk R, Koch M (2007) Highly accurate optical material parameter determination with THz time-domain spectroscopy. Opt Express 15:4335

58. Scheller M, Jansen C, Koch M (2009) Analyzing Sub-100-Mm samples with transmission terahertz time domain spectroscopy. Opt Commun 282:1304
59. Dorney TD, Baraniuk RG, Mittleman DM (2001) Material parameter estimation with terahertz time-domain spectroscopy. J Opt Soc Am A 18:1562
60. Duvillaret L, Garet F, Coutaz J-LL (1996) A reliable method for extraction of material parameters in terahertz time-domain spectroscopy. IEEE J Sel Top Quantum Electron 2:739
61. Angrisani L, Cavallo G, Liccardo A, Papari G, Andreone A (2016) THz Measurement Systems. In: Cocco L (ed) New Trends and Developments in metrology. InTech, London
62. Banhegyi G (1988) Numerical analysis of complex dielectric mixture formulae. Colloid Polym Sci 266:11
63. Smith NV (2001) Classical generalization of the Drude formula for the optical conductivity. Phys Rev B 64:155106
64. Withayachumnankul W, Naftaly M (2014) Fundamentals of measurement in terahertz time-domain spectroscopy. J Infrared Millimeter Terahertz Waves 35:610
65. Baxter JB, Schmuttenmaer CA (2006) Conductivity of ZnO nanowires, nanoparticles, and thin films using time-resolved THz spectroscopy. J Phys Chem B 110:25229–25239
66. Papari GP, Silvestri B, Vitiello G, de Stefano L, Rea I, Luciani G, Aronne A, Andreone A (2017) Morphological, structural, and charge transfer properties of F-doped ZnO: A spectroscopic investigation. J Phys Chem C 121:16012
67. Titova LV, Cocker TL, Cooke DG, Wang X, Meldrum A, Hegmann FA (2011) Ultrafast Percolative transport dynamics in silicon nanocrystal films. Phys Rev B 83:1
68. Fabian D, Brunner J, Schneider A, Gunter P (2009) A terahertz time-domain spectrometer for simultaneous transmission and reflection measurements at normal incidence. Opt Express 17:20685
69. Wang H, Guo JQ, Zhou YS (2013) Understanding terahertz optical properties of amorphous carbon thin films. Carbon 64:67
70. Nemilentsau AM, Shuba MV, D'yachkov PN, Slepyan GYA, Kuzhir PP, Maksimenko SA (2010) Electromagnetic response of the composites containing chemically modified carbon nanotubes. J Phys Conf Ser 248:012003
71. Dadrasnia E, Lamela H, Kuppam MB, Garet F, Coutaz J-L (2014) Determination of the DC electrical conductivity of multiwalled carbon nanotube films and Graphene layers from noncontact time-domain terahertz measurements. Advances in Condensed Matter Physics 2014:370619
72. Titantah JT, Lamoen D (2004) Determination of the electron effective band mass in amorphous carbon from density functional theory calculations. Phys Rev B 70:033101
73. Kam K-K (1982) Electrical properties of WSe_2, WS_2, $MoSe_2$, MoS_2, and their use as photoanodes in a semiconductor liquid junction solar cell. PhD thesis, Iowa State University, Ames, IA, USA
74. Ma Y, Kolekar S, Diaz HC, Aprojanz J, Miccoli I, Tegenkamp C, Batzill M (2017) Metallic twin grain boundaries embedded in MoSe 2 monolayers grown by molecular beam epitaxy. ACS Nano 11:5130
75. Papari GP, Koral C, Hallam T, Duesberg GS, Andreone A (2018) Terahertz spectroscopy of amorphous WSe2 and MoSe2 thin films. Materials 11:1613
76. Pereira MF, Winge D, Wacker A, Zubelli JP, Rodrigues AS, Anfertev V, Vaks V (2017) Theory and measurements of harmonic generation in semiconductor Superlattices with applications in the 100 GHz to 1 THz range. Phys Rev B 96:045306
77. Pereira MF (2018) Analytical expressions for numerical characterization of semiconductors per comparison with luminescence. Materials 11:1–15
78. Apostolakis A, Pereira MF (2019) Controlling the harmonic conversion efficiency in semiconductor superlattices by interface roughness design. AIP Adv 9:015022
79. Apostolakis A, Pereira MF (2019) Numerical studies of superlattice multipliers performance. Quantum Sens Nano Electron Photonics XVI:109262

80. Apostolakis A, Pereira MF (2019) Potential and limits of superlattice multipliers coupled to different input power sources. J. Nanophotonics 13:036017
81. Pereira MF (2016) The linewidth enhancement factor of intersubband lasers: from a two-level limit to gain without inversion conditions. Appl Phys Lett 109:222102
82. Pereira MF, Faragai IA (2014) Coupling of THz radiation with intervalence band transitions in microcavities. Opt Express 22:3439
83. Pereira MF, Anfertev V, Zubelli JP, Vaks V (2017) THz generation by GHz multiplication in superlattices. J Nanophotonics 11:046022
84. Winge DO, Franckié M, Verdozzi C, Wacker A (2016) Simple electron-electron scattering in non-equilibrium Green's function simulations. J Phys Conf Ser 696:012013
85. Pereira MF, Shulika O (2014) Terahertz and mid infrared radiation: detection of explosives and CBRN (using terahertz), NATO science for peace and security series-B: physics and biophysics. Springer, Dordrecht
86. Pereira MF, Shulika O (2011) Terahertz and mid infrared radiation: generation, detection and applications, NATO science for peace and security series-B: physics and biophysics. Springer, Dordrecht
87. Apostolakis A, Pereira MF (2020) Superlattice nonlinearities for gigahertz-terahertz generation in harmonic multipliers. Nano 9(12):3941–3952. https://doi.org/10.1515/nanoph-2020-0155
88. Pereira MF, Anfertev V, Shevchenko Y, Vaks V (2020) Giant controllable gigahertz to terahertz nonlinearities in superlattices. Sci Rep 10:15950